

# Ultrafast optical spectroscopy of semiconducting and plasmonic nanostructures and their hybrids.

Daniele Catone<sup>1</sup>, Lorenzo Di Mario<sup>1</sup>‡, Faustino Martelli<sup>2</sup>,  
Patrick O’Keeffe<sup>3,\*</sup>, Alessandra Paladini<sup>3</sup>, Jacopo Stefano Pelli  
Cresi<sup>3</sup>§, Aswathi K. Sivan<sup>2</sup>, Lin Tian<sup>2</sup>||, Francesco Toschi<sup>3</sup>,  
Stefano Turchini<sup>1</sup>

<sup>1</sup> Istituto di Struttura della Materia-CNR (ISM-CNR), Division of Ultrafast Processes in Materials (FLASHit), 100 Via del Fosso del Cavaliere, 00133 Rome, Italy.

<sup>2</sup> CNR-IMM, Area della Ricerca di Roma Tor Vergata, 100 Via del Fosso del Cavaliere, 00133 Rome, Italy.

<sup>3</sup> Istituto di Struttura della Materia-CNR (ISM-CNR), Division of Ultrafast Processes in Materials (FLASHit), 00015 Monterotondo Scalo, Italy.

E-mail: \*patrick.okeeffe@ism.cnr.it

**Abstract.** The knowledge of the carrier dynamics in nanostructures is of fundamental importance for the development of (opto)electronic devices. This is true for semiconducting nanostructures as well as for plasmonic nanoparticles (NPs). Indeed, improvement of photocatalytic efficiencies by combining semiconductor and plasmonic nanostructures is one of the reasons why their ultrafast dynamics are intensively studied. In this work, we will review our activity on ultrafast spectroscopy in nanostructures carried out in the recently established EuroFEL Support Laboratory. We have investigated the dynamical plasmonic responses of metal NPs both in solution and in 2D and 3D arrays on surfaces, with particular attention being paid to the effects of the nanoparticle shape and to the conversion of absorbed light into heat on a nano-localized scale. We will summarize the results obtained on the carrier dynamics in nanostructured perovskites with emphasis on the hot-carrier dynamics and in semiconductor nanosystems such as ZnSe and Si nanowires, with particular attention to the band-gap bleaching dynamics. Subsequently, the study of semiconductor-metal NP hybrids, such as CeO<sub>2</sub>-Ag NPs, ZnSe-Ag NPs and ZnSe-Au NPs, allows the discussion of interaction mechanisms such as charge carrier transfer and Förster interaction. Finally, we assess an alternative method for the sensitization of wide band gap semiconductors to visible light by discussing the relationship between the carrier dynamics of TiO<sub>2</sub> NPs and V-doped TiO<sub>2</sub> NPs and their catalytic properties.

‡ present address: University of Groningen, Groningen, The Netherlands

§ present address: Sincrotrone Trieste S.C.p.A., Trieste, Italy

|| present address: Institute for Quantum Computing and Department of Electrical and Computer Engineering, University of Waterloo, ON N2L 3G1, Waterloo, Canada

## 1. Introduction

The study of hybrid nanostructured semiconductor and plasmonic materials has undergone an explosion in the recent years largely thanks to the hope of improving the performances of semiconductor devices and materials by taking advantage of the strong light/matter interaction of the plasmonic nanomaterials [1, 2, 3]. A particularly fertile area of research is the sensitization of wide band gap semiconductors to visible light by this method. For example, transition metal oxide catalysts such as  $\text{TiO}_2$  and  $\text{ZnO}$  have band gaps larger than 3 eV which means that they can only absorb light in the UV region of the spectrum which contains  $< 5\%$  of the solar energy. This means that the efficiency of photocatalysis by such materials averaged over the entire spectrum is intrinsically low. This limitation has largely blocked the widespread use of these materials for green photocatalysis methods such as water splitting,  $\text{CO}_2$  reduction and water disinfection [4, 5, 6]. Furthermore, in recent years there is a growing interest in employing plasmonic hot electrons in hybrid devices for sensing, photodetection and solar energy applications [7].

The physical basis for the strong light matter interaction of plasmonic nanoparticles (NPs) is that at certain (resonant) wavelengths the conduction electrons in the nanostructure start to oscillate in resonance with the frequency of the light. Thanks to this localized surface plasmon resonance (LSPR) an extremely intense local concentration of the electric field of the light into “hot spots” is achieved. The order of magnitude of the field enhancement is expressed by the so-called quality factor  $Q = \omega/2\gamma$  [8], where  $\omega$  is the angular frequency of the plasmon resonance and  $\gamma$  is the total decay rate. It should be noted that the relaxation dynamics plays a fundamental role in engineering plasmonic devices. Furthermore, these objects exhibit extremely large absorption and scattering cross sections which can be up to 5 orders of magnitude larger than common organic dye molecules for example [9].

Incorporating plasmonic materials into semiconductor nanostructures aims to take advantage of these large absorption/scattering cross sections by any one of a number of different mechanisms such as: i) light trapping, ii) near-field electromagnetic field concentration iii) resonant energy transfer, iv) indirect hot electron injection and v) direct decay of a hybridized plasmonic/semiconductor state into the semiconductor [5]. Light trapping can occur by multiple scattering events within a 3D plasmonic nanostructure thanks to the large scattering cross-sections. This leads to an increased absorption path and thus to higher extinction efficiency. Near-field electromagnetic field concentration can be viewed as light concentration due to the effect of the plasmon oscillation. The result is increased absorption near the surface of the plasmonic material and can be taken advantage of by physically putting the plasmonic and semiconductor materials in contact. The resonant energy transfer can be mediated by dipole-dipole coupling leading to the transfer of energy between these dipoles. This interaction, which has long been known to take place between donor and acceptor molecules, is known as Förster Resonant Energy Transfer (FRET) and can also take place in hybrid

plasmonic/semiconductor nanostructures [10, 11]. All of these mechanisms require a spectral overlap of the absorption in the two materials. On the other hand the last two mechanisms do not require such overlap and the semiconductor can be excited by decay of the plasmonic state. In the case of the indirect hot electron injection the decay of the plasmon produces a non-thermal electron distribution in the plasmonic structure. This can be followed by injection of electrons over a Schottky barrier formed at the plasmonic material/semiconductor interface and is also referred to as an internal photoemission process. The channels for the formation of hot electrons are [12]: free carrier absorption arising from phonon and defect scattering, absorption assisted by electron-electron scattering, absorption via Landau damping. In the latter, hot electrons are generated in the near surface region by a surface collisions assisted mechanism and they have a good average directionality with respect to the electric field. Landau damping is considered the more promising channel to overcome the Schottky barrier and to inject hot electrons in the semiconductor. This kind of damping is particularly efficient in nanoparticles whose size is less than the mean electron path. In the direct decay mechanism the plasmon can dephase into empty hybridized orbitals formed at the interface between the plasmonic and semiconductor materials [13]. If these orbitals have significant semiconductor character the result is direct formation of hot electrons in the semiconductor as a result of decay of the plasmon.

Which one of these mechanisms, if any, dominates depends on a large number of factors including: i) alignment of the bands of materials, ii) excitation wavelength, iii) morphology of the materials, iv) the presence and location of hotspots, v) the relative strength of absorption and scattering of the plasmonic material vi) structure of the interface, and vii) the presence and type of defects in the semiconductor material, to name just a few.

In our work we study these interactions by monitoring the temporal evolution of the optical response of the materials following photoexcitation. To be able to understand and correctly interpret the response of the hybrid systems it is clearly necessary to first understand the response of the individual plasmonic and semiconductor materials. The ultrafast processes in the two materials are quite different so we will discuss them separately.

The optical response of metal nanoparticles have been extensively studied over the years [14]. Following the photoexcitation of the LSPR of a plasmonic nanostructure, the energy absorbed by the nanoparticle is transferred from the oscillating electrons of the plasmon to conduction electrons mainly by Landau damping resulting in a non-thermal energy distribution of the electrons above and below the Fermi level on timescale of tens of femtoseconds. The resulting energetic electrons then undergo a thermalization process through electron-electron scattering to produce a Fermi-Dirac energy distribution characterized by a temperature of hundreds to thousands of Kelvin depending on the energy and intensity of the exciting light. This process generally takes place within hundreds of femtoseconds. Subsequently, this hot electron distribution undergoes cooling mainly by electron-phonon coupling in which energy is transferred

to the lattice of the plasmonic nanostructure within several picoseconds. Finally, the plasmonic nanostructure exchanges energy with the surrounding materials through phonon-phonon coupling typically on the scale of hundreds of picoseconds. The precise timings of these processes are strongly dependent on the quantity of energy deposited in the nanostructure during the laser pulse, with the processes generally taking longer for higher intensity excitation. All of these processes can be monitored by measuring the optical response of the plasmonic nanostructures in time as will be discussed below. In addition to the above processes, competing phenomena can take place when the intensity of the exciting light is raised above a threshold which can result in modification of the morphology of the nanostructures or non-linear processes.

In a nanostructured semiconductor, absorption of light with energy above the band gap of the material leads to promotion of an electron from the valence band to the conduction band, resulting in the formation of an electron-hole pair. In the case in which the energy of the photon is significantly above the band gap, a very energetic non-thermal distribution of charge carriers is produced. This distribution rapidly thermalizes through carrier-carrier scattering on the 100s of femtoseconds timescale thus allowing the energy distribution to be described by a Fermi-Dirac distribution with a well defined temperature. Subsequently, energy relaxation to the band edges can take place by emission of optical phonons on the picosecond timescale. The signals can also decay via three body Auger-type processes, band-to-band recombination and trap-assisted (Schokley-Read-Hall) recombination, each of which have characteristic lifetimes. The time-dependent carrier density can be monitored down to the femtosecond timescale by following the bleaching of the band edge absorption in transmission experiments.

These dynamics are strongly dependent on the excitation intensity and thus the initial carrier density. For example, many body effects such as band gap renormalization can lead to a time-dependent red-shift of the band edge. Other intensity dependent dynamics include band filling which leads to a time-dependent blueshift of the absorption edge and non-equilibrium phonon populations which can slow the relaxation of the carriers (hot-phonon bottleneck). Clearly, also the band-to-band and Auger recombination processes depend on the carrier density. Furthermore, the dynamics can depend strongly on the defect density of the semiconductor as trapping and trap-assisted decay can modify the lifetimes of the carriers. An excellent review on the carrier and phonon dynamics in semiconductors can be found in [15].

As can be seen from the above discussion, the dynamics of both the plasmonic nanoparticles and the semiconductor nanostructures on the femtosecond timescales are both complicated and intensity dependent and can be influenced by numerous factors. To gain some insight into the extraction of reliable information on these dynamics from optical pump-probe methods we structure this article in the following manner: first, Transient Absorption (TA) spectroscopy (the main experimental optical technique used in our studies) is briefly described, we then summarize some of our measurements on plasmonic metal nanoparticles [16, 17, 18, 19], this is followed by a discussion of the dynamics extracted from our optical measurements on a range of nanostructured

semiconductors [20, 21, 22], we then analyze the dynamics in hybrid systems [23, 24] with the aim of achieving an understanding of the parameters governing the modification of the dynamics due to interactions in these systems and, finally, we describe the carrier dynamics of TiO<sub>2</sub> NPs and V-doped TiO<sub>2</sub> NPs and how they affect their catalytic properties.

## 2. Methods

### 2.1. Ultrafast transient absorbance spectroscopy

Ultrafast TA spectroscopy pump-probe measurements were all performed using a femtosecond laser system consisting of an oscillator (20 fs pulse duration, 80 MHz repetition rate, 550 mW power centred at 800 nm) that seeds a regenerative amplifier thus producing 35 fs pulses at 1 KHz with 4 mJ peak power. The pump pulses are produced by using the output of an optical parametric amplifier in the 240 - 1600 nm wavelength range. The probe is a white light supercontinuum beam (250 - 1550 nm) that is generated in a commercial TA spectrometer (FemtoFrame II, IB Photonics) using three different setups depending on the energy range to be covered (UV, visible, and IR): the UV probe (240 - 370 nm) is generated by focusing a 400 nm laser beam into a rotating CaF<sub>2</sub> crystal; the visible probe (360 - 780 nm) is generated by focusing an 800 nm pulse into a rotating CaF<sub>2</sub> crystal; the IR probe (850 - 1550 nm) is generated by focusing an 800 nm pulse into a YAG crystal. The TA spectroscopy experiments are performed using a pump and a probe beam focused on the sample (pump diameter = 300  $\mu$ m; probe diameter = 150  $\mu$ m) and modifying the delay time between the two by changing the optical path of the probe. In the case of the UV and visible probe, the beam is split into two with a half collected by the first spectrometer and used as reference to account for pulse to pulse fluctuations in the white light generation. The remaining half probe beam is collected by the second spectrometer after being transmitted or reflected by the sample. In IR probe a single spectrometer is used. The differences in absorbance (reflectance) of the sample when excited by the pump and when unperturbed, i.e. the transient absorbance  $\Delta A$  (transient reflectance  $\Delta R$ ), are measured as a function of the pump-probe delay time. These setups allow both liquid and solid samples to be investigated with an instrument response function of about 50 fs. Moreover, the solid samples can be measured in air at room temperature or under vacuum at 77K. More details can be found elsewhere [22, 23].

## 3. Results and discussion

### 3.1. Ultrafast Optical Response of Nanostructured Plasmonic Materials

#### 3.1.1. Gold Nanoparticles in Solution

The optical response of plasmonic materials following photoexcitation can be best illustrated by pump-probe studies on gold spherical nanoparticles. Figure 1a reports the

false-color TA map of a water solution of 10 nm citrate capped Au NPs (0.05 mg/ml), when excited by a 370 nm pump beam with a fluence of  $150 \mu\text{J}/\text{cm}^2$ . The map is characterized by a strong negative feature around 520 nm and two positive wings on both sides, the one on the blue side being much more intense. These features are due to the alterations of the optical properties of the Au NPs upon excitation by the femtosecond pump beam. Following irradiation, the electrons heat up [14] causing a depletion and broadening of the plasmon resonance. As a result, a (negative) photobleaching (PB) of the probe signal and the appearance of two positive wings on either sides of the bleaching is observed in the TA map [25].

During the first few hundreds of femtoseconds, the features of these signals moves to shorter wavelengths and increases until the nascent non-thermal electron distribution has thermalized to a hot distribution. After reaching their maximum values, the signals of both the bleaching and the positive wings decrease in a few picoseconds, mainly due to electron-phonon coupling [14]. Finally, a long timescale decay is observed, as the NP returns to its unperturbed state on a timescale of tens/hundreds of picoseconds through phonon-phonon scattering processes.

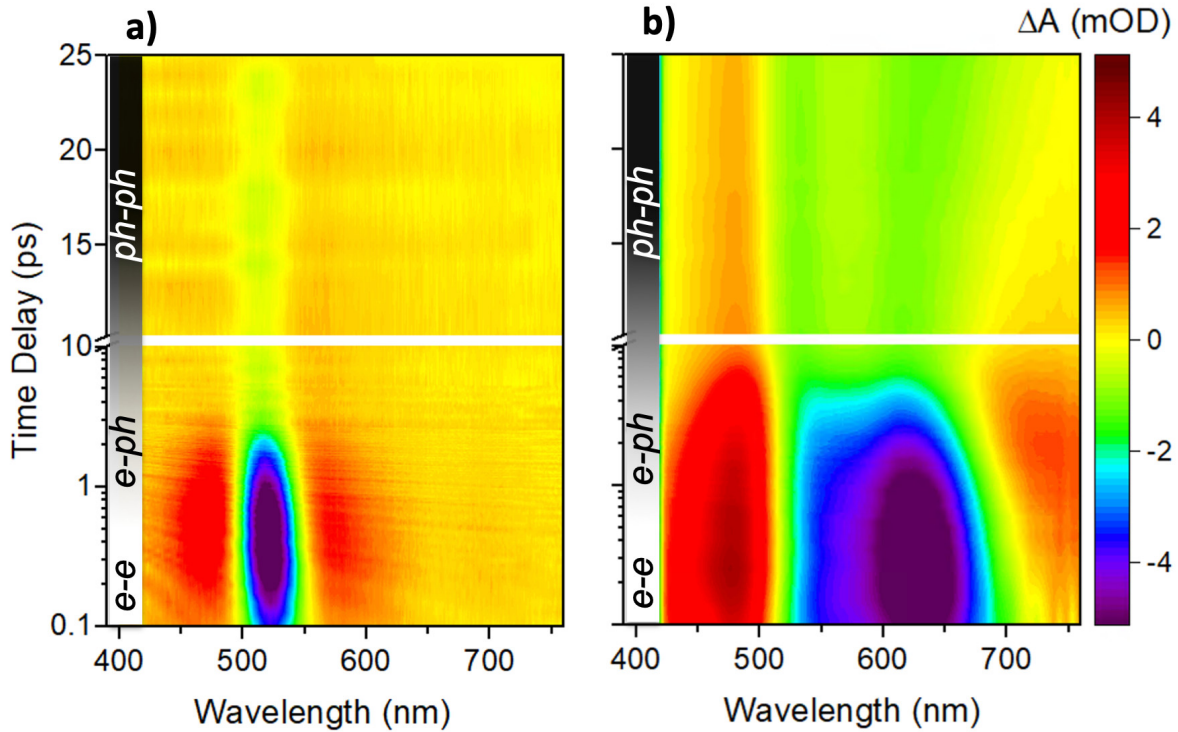


Figure 1 Transient absorption map of a water solution of: a) 10 nm citrate capped gold spherical NPs excited with a 370 nm pump, b) 10 nm gold spherical NPs, functionalized by rhodamine B isothiocyanate (Au@RITC) [16] excited with a 400 nm pump. On the left of each map, a vertical stripe indicates the temporal range of the subsequent scattering (e-e, e-ph, ph-ph) events following photoexcitation of the nanostructure

As is well known, the wavelength position and bandwidth of LSPRs depend on a number of factors, including the size, shape and composition of the plasmonic



materials [26]. As visible in figure 1a, spherical NPs exhibits only a single (transverse) LSPR due to their high-order symmetry, while NPs with different symmetries present more LSPR modes [27, 28].

Interesting effects are also observed when NPs approach each other and interact. We studied 10 nm gold spherical NPs, functionalized by rhodamine B isothiocyanate (Au@RITC) [16]: by modulating the quantity of dye molecules on the surface of the nanoparticles, and in turn the dielectric constant of the material between the nanoparticles, it was possible to exploit the coupling of plasmonic resonances between closely spaced NPs [29, 30]. Such a coupling can be described in terms of a delocalization of the plasmon resonance over a number of particles [31, 32], leading to the appearance of an additional extended LSPR. Figure 1b shows the false-colour TA map of the Au@RITC water solution, when excited by a 400 nm pump beam with a fluence of  $180 \mu\text{J}/\text{cm}^2$ . The bleaching of both the transverse and extended LSPRs are observable, around 530 nm and 630 nm, respectively. The broadness of the extended LSPR suggests the presence of many substructures [16], such as chains of different length, bidimensional nanoaggregates, and so on.

### 3.1.2. 3D Arrays of Gold Nanoparticles deposited on $\text{SiO}_2$ Nanowires

We now discuss how the simple deposition of the plasmonic NPs on the surface of the semiconductor may change the properties of the metallic NPs themselves. This is particularly true when NPs are deposited on the sidewalls of nanowires (NWs). The reason for changing the plasmonic characteristics is that the NW sidewalls induce a NP shape that is not spherical or hemispherical, but ellipsoidal. The silica NW arrays have been fabricated via thermal oxidation of Si NWs grown on a quartz substrate. The silica NWs are an excellent support for metal NPs because they provide a large surface area to attach the NPs and, at the same time, a macroporous framework that ensures an efficient interaction with the environment. The arrays are also fully transparent in the visible to near-UV region of the spectrum, which helps the characterization of the NPs because allows the measurements in transmission. Additionally, the strong light scattering typical of the nanowire-based structures increases the light absorption of the NPs. Silica NW arrays have been decorated with both Au [19] and Ag NPs, which have been obtained by dewetting thin metallic films evaporated on top of the NWs [33].

In figure 2 the spectral dependence of the transient absorbance at different pump-probe delay times is reported for both Au (figure 2a) and Ag-decorated silica NWs (figure 2b). As expected, the spectra show a decrease of the TA signal at the LSPR immediately after the pump excitation. For the Ag NPs both the dipole and quadrupole contribute to the plasmon resonance. All the probe energies show similar dynamics, indicating that a single process is dominant in this time range: the electron-phonon coupling. An interesting feature of our results is the blue-shift of the TA resonance bleaching for increasing delay time. This feature is unusual for homogeneous distributions of metallic NPs and we have attributed it to the shape distribution of the Au and Ag NPs resulting from the dewetting method used to fabricate them. Using a three-temperature model

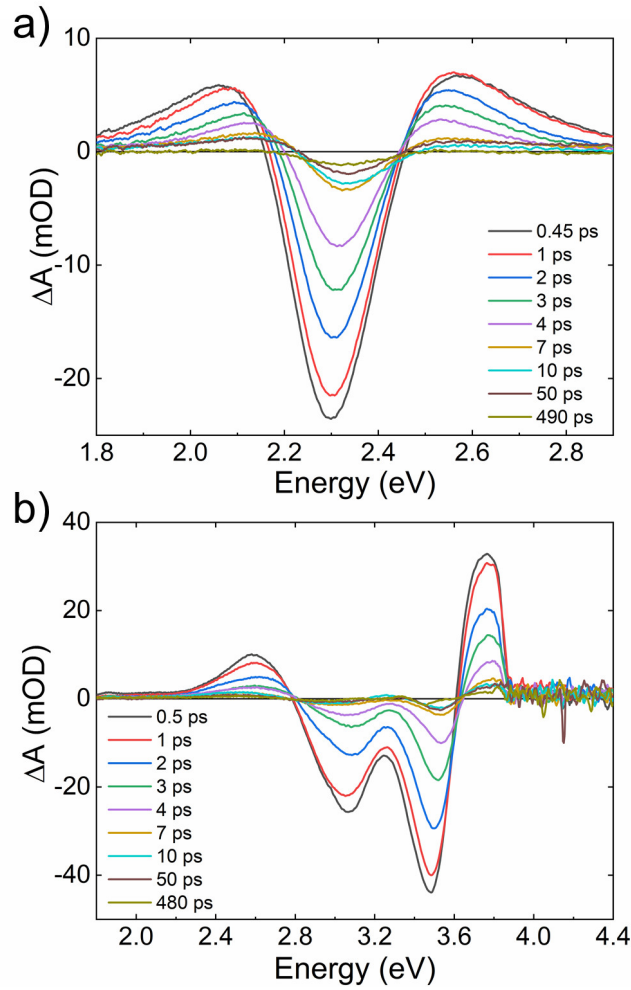


Figure 2 Transient absorbance spectra at different pump-probe delay time for metal NPs on silica NWs: a) Au NPs, b) Ag NPs.

(3TM) [19] that includes the electron  $T_e(t)$  and lattice  $T_l(t)$  temperatures of the NPs and the temperature of the surrounding environment  $T_{env}(t)$ , we have observed that to account for the observed shift we had to consider the NP shape and its distribution. In particular, for Au NPs, we have considered oblate NPs with different aspect ratio to be the closest picture to the real shape distribution obtained with our sample preparation. In figure 3a a graphic representation of the shape distribution used for the simulations can be found.

Thanks to our simulations (figure 3b) that account for the real shape distribution of our NPs, we have been able to assign several characteristics observed in the experimental transient optical response to the effect of the distribution of the NP shape. In particular, the profile of the two positive wings is strongly related to the shape and to the shape distribution of the NPs, as expected from the observation of quite different behaviors in spherical and rodlike NPs [34, 35, 36]. The figure 3b shows that at a given delay time the position of the absorption bleaching is different for different aspect ratios of the



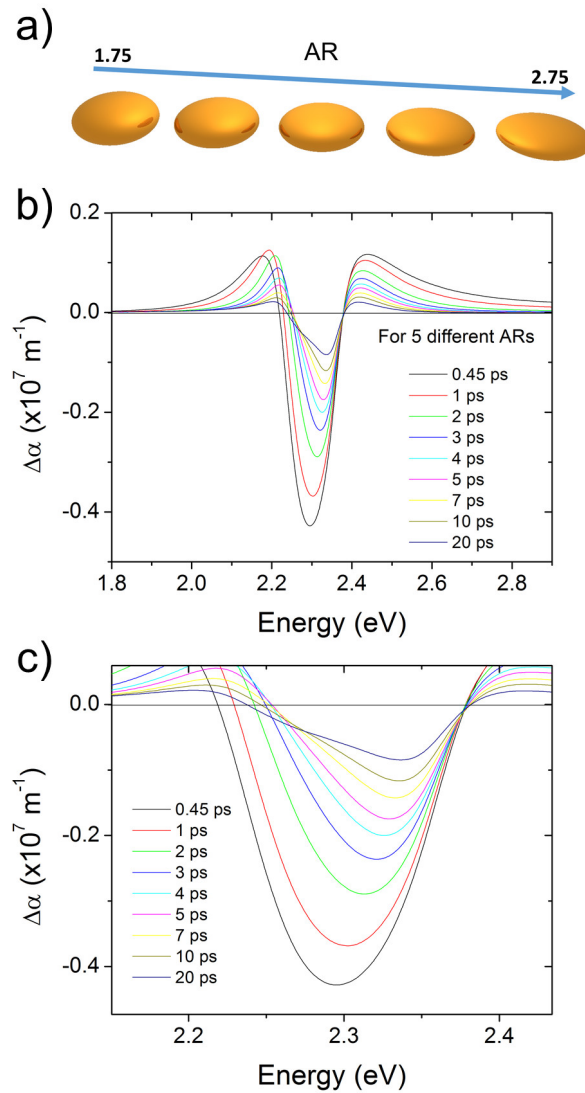


Figure 3 a) Graphic representation of the five aspect ratios (1.75, 2.00, 2.25, 2.50, and 2.75) considered for the oblate Au NPs. b) Calculated spectral dependence of  $\Delta A$  for NPs with different ARs and their average value at 4 ps delay. c) Close-up of bleaching position, which shows the blueshift with increasing delay time.

oblate. When the shape distribution is then considered in the simulation of the overall system, the result shows a blue shift of the bleaching position for increasing pump-probe delay times, as shown in figure 3c. The shape distribution, that has been accurately calculated for Au NPs [19], is assumed to be the reason for the similar blue-shift of the LSPR bleaching observed for Ag NPs.

These observations have important consequences when examining the transient responses of mixed NP/semiconductor systems: ultrafast changes in the spectral response of the LSPR bleaching may not be related to ultrafast energy transfer processes between the materials but may simply be due to wide morphological distributions of NPs within the sample.

### 3.1.3. Thermal Effects in the Optical Excitation of Plasmonic Materials

As can be seen from the above discussion most of the energy absorbed by plasmonic materials such as metal NPs gets rapidly converted into heat. While it can be interesting to deposit heat in a controlled manner on the nanometer scale [37], in mixed plasmonic/semiconductor systems aimed at transferring absorbed energy from the plasmonic material to the semiconductor it is an undesirable process. In a simple energy balance equation the energy absorbed by the plasmonic material but not converted into heat has been transferred to the surrounding material. The latter is the desired process in the above plasmonic/semiconductor system. Therefore, in this section we discuss methods to measure the quantity of energy deposited as heat in metal NPs systems and how different types of exciting light deposit thermal energy in different ways.

With these concepts in mind we have developed a method to determine the time dependent temperature of the NPs in the relaxation processes after an ultrashort pulse excitation. The electronic temperature ( $T_e$ ), lattice temperature ( $T_l$ ), and environmental temperature ( $T_{env}$ ) are the basic ingredients of theoretical models such as two and three temperature models [38] such as that described above for the 3D arrays of AuNPs on SiO<sub>2</sub> nanowires [19]. Generally, the temperature of the NPs are extrapolated indirectly from experimental data by comparison of the pump-probe transient absorption to the results of these models. In our work [39] a simple method to estimate the temporal evolution of the temperature has been proposed and demonstrated on self-organized 2D arrays of ellipsoidal AuNPs deposited onto the surface of a LiF single crystal substrate [40]. The result was achieved by comparing data obtained from the temporal evolution of the transient photobleaching peak and the static absorption spectra of the AuNP system immersed in a thermodynamic bath where the temperature ( $T_{bath}$ ) is known. In the latter case by definition  $T_e = T_l = T_{env} = T_{bath}$ . Overlapping the two experimental datasets it was possible to determine a good match between the dynamic and static data associating a temperature with a delay time as shown in (figure 4 a). It should be noted that for times below 10 ps the static data do not match with dynamic ones, thus suggesting that it is the temporal lower limit of the method. The main reason for this is that at these delay times  $T_e$  and  $T_l$  are still strongly out of equilibrium because the system is still transferring the energy/heat from electrons to the lattice. By fitting the data from the longer times ( $> 10$ ps) with a linear function and projecting this onto the data of the lower  $T_{bath}$  static points it was possible to build an effective thermometric scale (figure 4b). Then the experimental TA points can be projected onto the calibration curve estimating the associated temperature. This method is not limited to the system of AuNPs described above but it is applicable to all systems where it is possible measure the ultrafast optical response and steady state spectral response at controlled temperature.

Having a method to extract the temperature of the NPs will be of use when evaluating the amount of absorbed energy which is converted into heat in hybrid

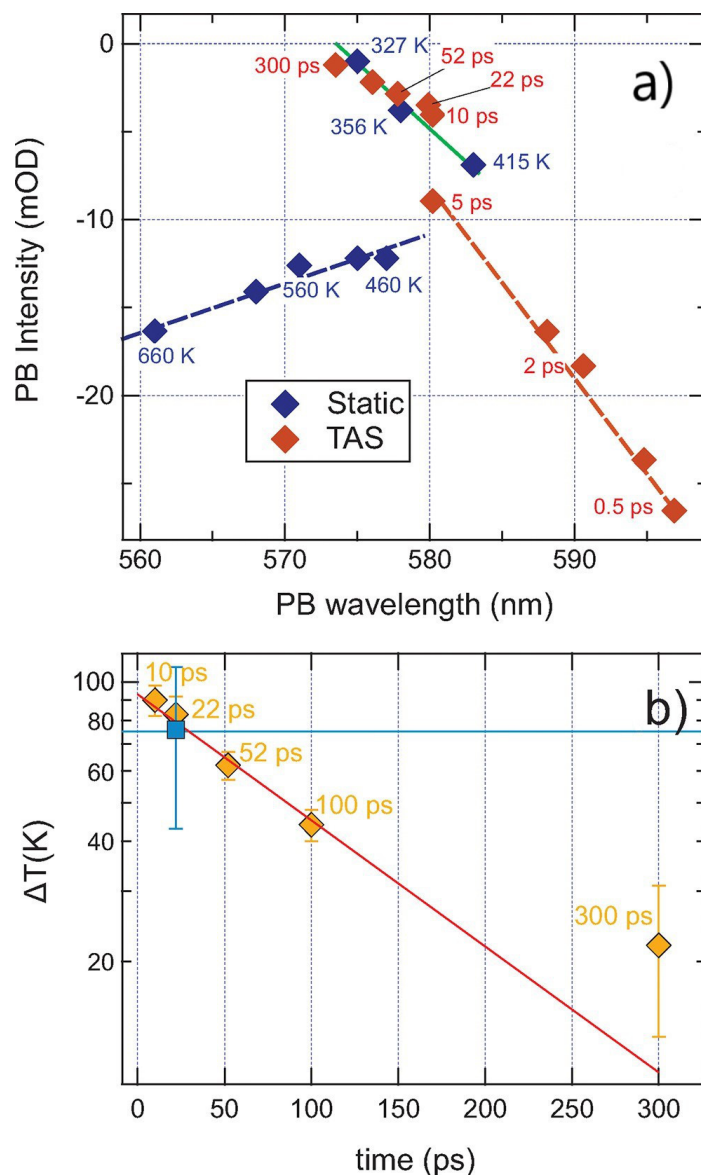


Figure 4 a) Plot of the photobleaching intensity against photobleaching wavelength extracted from the dynamics of the TA spectra (red markers) and those extracted from static  $T_{bath}$ -dependent data (blue markers). The values of  $\tau$  and  $T_{bath}$  of each point is indicated in the figure. The dashed lines act as a guide to the eye while the continuous green line is an interpolation of the static data in the 415-327 K  $T_{bath}$  range. b) The NP temperature extracted from the analysis of the data in panel a) (orange symbols) plotted as a function of time together with the estimated low-delay NP temperature (blue symbols). The red line shows an exponential fit to the orange points. Reprinted and adapted with permission from [39]. Copyright (2020) American Chemical Society.

plasmonic/semiconductor systems as it may provide a tool to evaluate how much energy is transferred from the NP to the semiconductor material in the first 100s of femtoseconds before the heating takes place.

Another related experiment we have performed on these 2D arrays of gold NPs is to compare the efficiency of different types of excitation, either interband transition ( $\lambda = 400$  nm) or plasmonic excitation ( $\lambda = 600$  nm), in converting absorbed energy

into thermal energy [18]. These experiments were performed at much higher excitation intensities as the method to determine heating efficiency was to examine permanent changes to the morphology and optical response of the NPs. At the high intensities used in this work the quantity of heat deposited can lead to melting, coalescence, and even ablation of the NPs. Figure 5a shows the transmission spectrum of the non-irradiated AuNP array where we mark in red the wavelengths of the incident laser radiation used in our experiment. At first glance one would expect the melting to be more efficient on plasmonic excitation due to the larger absorption at this wavelength (see transmittance measurements in figure 5a) confirmed by comparison with theoretical modelling which found absorption cross sections of  $\sigma_{abs}(400 \text{ nm}) = 2.03 \cdot 10^{-16} \text{ m}^2$  and  $\sigma_{abs}(600 \text{ nm}) = 3.45 \cdot 10^{-16} \text{ m}^2$ , respectively, for these arrays [18].

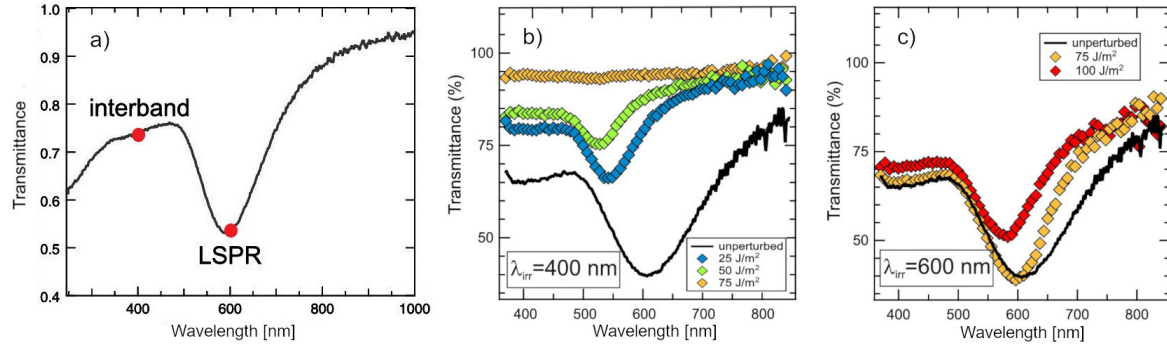


Figure 5 a) Transmission spectrum of a pristine 2D AuNP array, red dots are the two excitation wavelengths b) Transmission spectra of the AuNP array after irradiation on the interband transition c) Transmission spectra of the AuNP array after irradiation on the LSPR excitation. Reprinted and adapted with permission from [18]. Copyright (2019) American Chemical Society.

However, in the experiment exactly the opposite was found as can be seen from the microtransmission spectra of the areas irradiated by different fluences of 400 nm (figure 5b) and 600 nm (figure 5c) radiations: for the fluence of  $75 \text{ J/m}^2$  the arrays are completely depleted by 400 nm radiation while only minor modifications of the transmission (and thus morphology of the AuNPs) occurs for the same fluence at 600 nm. These observation were confirmed by the AFM images of the irradiated areas [18]. This unexpected behavior can be explained by taking into account the different distribution of the electric field in the NPs between the plasmonic and interband cases. Indeed, for interband excitation the electric field magnitude is relatively homogeneous, whereas for plasmonic interaction the electric field magnitude become strongly inhomogeneous with a strong concentration on the small portion of the NPs facing the interparticle gap (hot spots). For homogeneous fields, the NPs undergo homogeneous heating and consequently high temperatures are achieved throughout the NPs. For the plasmonic case, the total amount of energy deposited is larger due to the larger absorption cross section. A possible explanation is that highly localized heating due to the hot spots leads to ultrafast non-thermal melting [41] and to the dissipation of the energy following different pathways such as local ablation of AuNP or the formation

of plasma in hot spot volume due to photoionization, impact ionization and/or strong-field photoemission [42, 43]. These phenomena do not lead to efficient melting of the NPs privileging only localized reshaping of them. This demonstrates that interband excitation is significantly more efficient than plasmonic excitation in melting, coalescing, and sublimating the NPs.

In the context of the present article these results are encouraging as they suggest that processes which compete with simple heating of the NPs can occur in the case of plasmonic excitation. Further research is required to identify and, eventually, optimize these processes.

For the final experiment we describe in this section we return to the 10 nm Au@RITC water solution described in the previous section. The reason for this is that the LSPR in these systems is broadened and shifted to the red (see figure 1b), with longer chains of NPs associated with higher red shifts. Therefore, by tuning the wavelength of the exciting light it should be possible to exert control over the spatial distribution of energy deposited. In this experiment we avoided too high laser fluences which may cause nanocavitation, explosive boiling of the water around the NPs or even fragmentation of the NPs [44] and chose fluences such that only small modifications of the morphology of the aggregates occur. The induced modifications were subsequently investigated by measuring the new optical response and by SEM microscopy with the aim of understanding how the spatial distribution of the thermal energy deposited varies with excitation wavelength. Figure 6 shows the TA of the non-irradiated Au@RITC water solution (black line), acquired at a pump-probe delay of 1 ps [17]. The other colored lines show the TA acquired after irradiation of the solution at different wavelengths, corresponding to selective excitation in the interband (400 nm) or extended LSPR (570 and 620 nm) region. The macroscopic effect of this selective excitation can be clearly observed looking at the colors of the not-irradiated or irradiated solutions obtained (see inset of Figure 6).

Through finite integral technique calculations [45] we have shown that the spatial distribution and extent of the light concentration is strongly wavelength dependent: while interband irradiation causes a more isotropic and homogeneous heating leading to the coalescence into larger spherical NPs, plasmonic irradiation leads to a strong localization of the electric field in the interparticle regions, with hot spots playing a key role in promoting melting effects [17]. Accordingly, by tuning the melting laser in the extended LSPR region, it was possible to selectively excite the different aggregate substructures present in the solution and thus choose the spatial distribution of the energy deposited.

This experiment, which shows that it is possible to spatially localize the deposition of energy within plasmonic nanostructures, is important to keep in mind when designing/fabricating hybrid plasmonic/semiconductor nanostructures aimed at maximising energy transfer from the plasmonic to the semiconductor material. Indeed, this is one of the reasons why embedding the plasmonic material in the semiconductor (see the AgNP@Ceria example below) may lead to high yield of energy transfer.

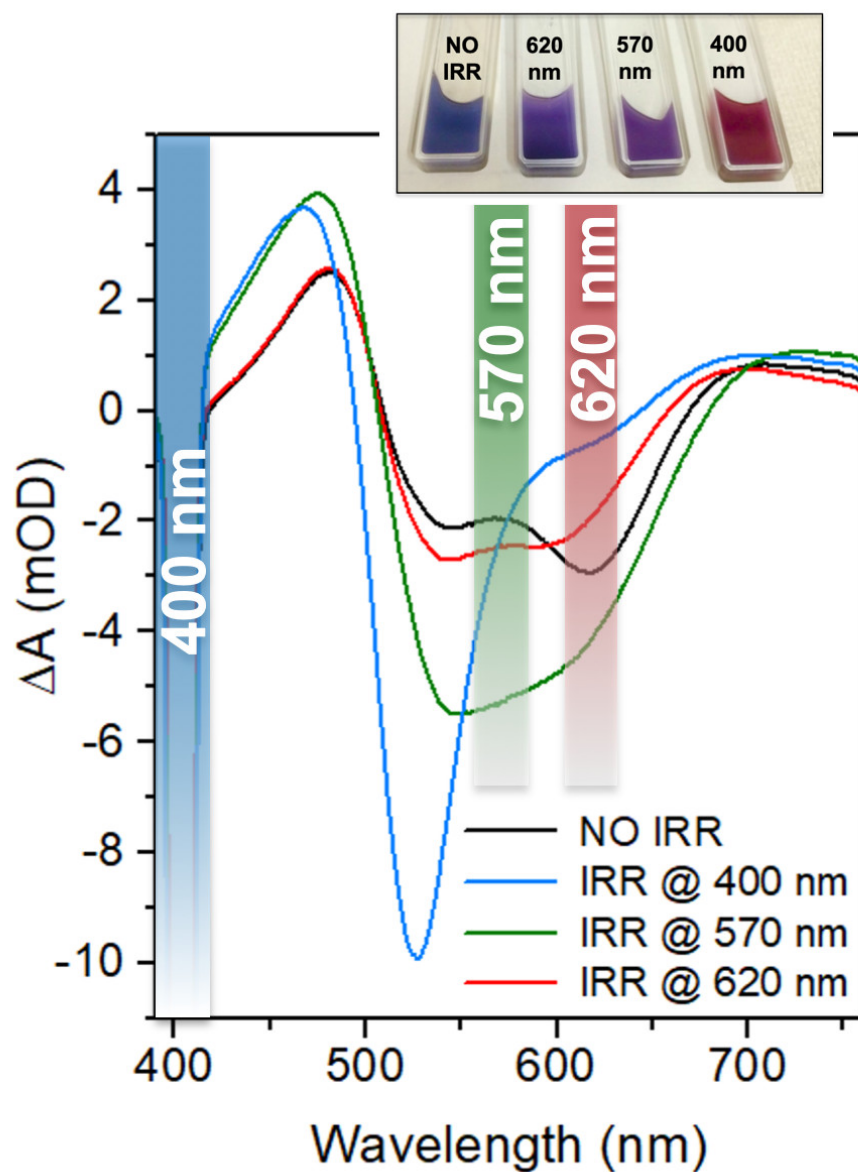


Figure 6 Effect of irradiance of the 10 nm gold spherical NPs, functionalized by rhodamine B isothiocyanate samples at different wavelengths on the transient absorption at a delay of 1 ps. The inset shows a photograph of the non-irradiated and irradiated samples thus illustrating the effect of irradiation on the steady state absorption.

### 3.2. Ultrafast Optical Response of Nanostructured Semiconducting Materials

#### 3.2.1. Nanostructured Halide Organic-Inorganic Perovskites

The morphology of polycrystalline films of semiconducting materials can have an important impact on the photoexcited carrier dynamics of the materials. An example where this effect can have consequences for the functioning of a semiconductor based device is in halide perovskite based solar cells (PSCs). The active layer of these devices is generally formed by spin coating precursor molecules of the perovskite on to a substrate



and allowing a crystallization process to form the perovskite layer. A major area of research is the investigation of the effect of the morphology of this layer on device performance and stability [46, 47, 48, 49]. In the case that we investigated [22] the precursor molecules were coated onto a mesoporous  $\text{TiO}_2$  (m- $\text{TiO}_2$ ) layer that acts as electron transport layer in the device. The result is a bilayer of perovskite consisting of a capping layer with large crystals (of  $\sim 500$  nm) and mesoporous layer with small crystals (20-40 nm) spatially restrained within the  $\text{TiO}_2$  mesoporous layer (see inset of figure 7a). It is possible to distinguish the transient optical responses of these layers as they have slightly different absorption edges [50] which leads to differences in their transient bleaching. The result is that photoexcitation of the large crystals leads to a bleaching signal centered at 1.64 eV ( $\text{PB}_{1A}$ ) while excitation of the small crystals produces a bleaching at 1.66 eV ( $\text{PB}_{1B}$ ) (see figure 7 a).

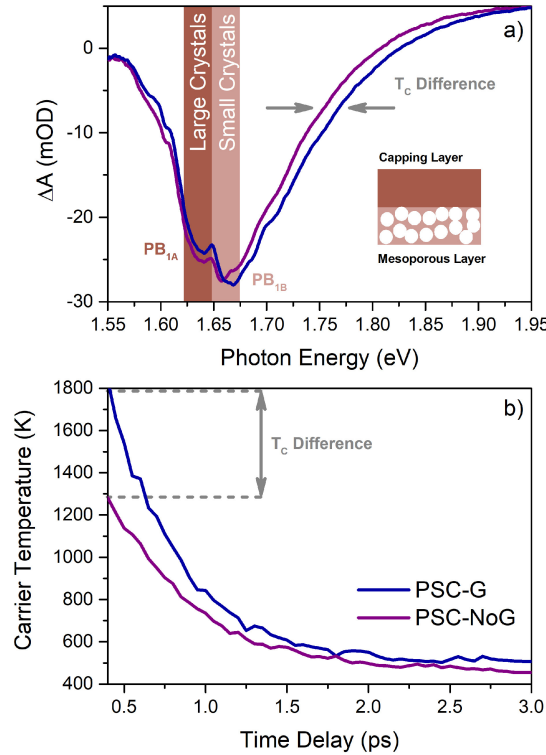


Figure 7 a) Transient absorption spectra acquired at 0.75 ps of time delay for 1-week aged PSC-G (blue line) and PSC-NoG (purple line). The photobleaching signal shows two distinct peaks at 1.64 eV ( $\text{PB}_{1A}$ ) and 1.66 eV ( $\text{PB}_{1B}$ ) assigned to the large crystals of the capping layer and the small crystals of the mesoporous layer, respectively. b) Carrier temperature as a function of time delay (from 0.4 to 3 ps) for 1-week aged PSC-G (blue line) and PSC-NoG (purple line). The cells were pumped at 3.1 eV with an initial carrier density of  $7.0 \times 10^{17} \text{cm}^{-3}$ .

The aim of our work was to study the effects of the addition of graphene flakes to the m- $\text{TiO}_2$  layer on the stability and carrier dynamics of these perovskite layers. To do so we measured the transient absorption of two PSCs with (PSC-G) and without (PSC-NoG) graphene, on fresh samples and after one week of shelf ageing. While the relative intensities of  $\text{PB}_{1A}$  and  $\text{PB}_{1B}$  are unchanged in the spectra of PSC-G with respect to

the as-prepared sample (data not shown [22]), they are different in PSC-NoG, suggesting that in PSC-NoG, a higher degradation of small crystals with respect to large crystals over time induces the intensity reduction of the  $PB_{1B}$  with respect to  $PB_{1A}$ .

Furthermore, the TA spectra presents another difference: the PB signal of PSC-NoG is less broadened (see gray arrows in figure 7a) with respect to that of the PSC-G, which remains unchanged after aging. This high-energy tail is directly related to the carrier temperature ( $T_C$ ) at a given time delay [51, 52]. In fact, it is possible to extract the  $T_C$  from the TA spectra by simply fitting the high-energy tail with a Maxwell-Boltzman function. This has been done and the  $T_C$  as a function of time for the 1-week aged PSC-G and PSC-NoG is shown in figure 7b. It can be seen that the initial  $T_C$  in the PSC-NoG (about 1300 K) is significantly lower than that in PSC-G (about 1800 K). This behavior indicates that the  $T_C$  difference arises from an overall faster thermalization of the carriers after excitation, occurring at time delays shorter than 0.4 ps. The conclusion is that the addition of graphene to the mesoporous layer protects the integrity of the small crystals, which in turn preserves the temperature of the carriers for a longer time after excitation.

### 3.2.2. ZnSe and Si Nanowires

Among semiconductor nanostructures, nanowires are of particular interest for the study of semiconductor-metal interactions because the large aspect ratio of these nanostructures offers a large surface for the deposition of metallic nanoparticles and a small diameter enabling the interaction to be spread over a large portion of the semiconductor making any ensuing effect more easily observable than in bulk or thin films [33]. NW arrays favor light trapping making light absorption more efficient because of the reduced reflectivity [53, 54, 55, 56]. This latter feature, along with the use of opaque substrates for the NW growth, make it difficult to perform transient reflectance or absorption measurements using conventional NW growth methods. In order to allow for transient absorption measurements, we have used NWs grown on transparent substrates. As these kinds of substrates do not withstand high temperatures, we turned our attention to materials that can be grown at low temperature with good optical quality, as ZnSe [57] and Si NWs [58]. This type of samples are semitransparent and allow for a good signal-to-noise ratio in the transient measurements [20, 21].

As mentioned in the introduction in time-resolved optical measurements of semiconductors the most typical spectral feature consists of a absorption bleaching at energies corresponding to excitonic or band gap transitions. This negative signal is due to decreased absorption at those energies induced by the photoexcited carrier population. This is clearly observed in both ZnSe and Si NWs, as shown in figure 8, with some important differences between the two materials. ZnSe is a direct gap material with a band gap of 2.6 eV at room temperature and we observe indeed a sharp bleaching signal at this energy (see the black arrow in figure 8), that is hence attributed to near band-edge (NBE) transitions. A broad bleaching signal is also observed at lower energies due changes in the absorption given by point defects, as usually also observed in

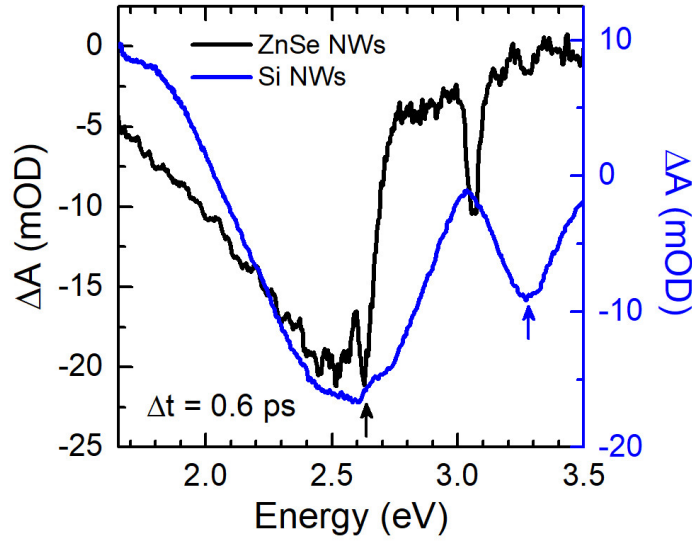


Figure 8 a) Transient absorption spectra acquired at a time delay of 0.6 ps by photoexciting a sample of ZnSe nanowires at 3.05 eV (black line) and a sample of Si nanowires (blue line) at 4.5 eV. The arrows indicate the energies of band edge bleaching. The sharp peak at 3.05 eV in the ZnSe nanowire spectrum is an artifact due to scattering of the pump radiation.

epitaxial ZnSe, that are reduced at low growth temperatures [59]. Si is an indirect gap material with energy of 1.1 eV, at which a clear absorption bleaching is not observed [21] while a strong and sharp bleaching is observed at 3.3 eV (see the blue arrow in figure 8), energy corresponding to the direct band gap of Si. The strong negative signal observed for Si below the direct band gap energy is due to the modification of the whole Si band structure upon photoexcitation [60]. Another difference between these two materials is the rise time of the bleaching signal. While for ZnSe we measure  $170 \pm 60$  fs [20], we are not able to measure it for Si as it is faster than the IRF of our set up. This latter finding is in agreement with what found by Schulze and coworkers, who measured the band gap shrinking occurring in hundreds attoseconds [61].

### 3.3. Energy Transfer in Hybrid Nanostructured Plasmonic/Semiconducting Materials

#### 3.3.1. 3D Arrays of Gold and Silver Nanoparticles deposited on ZnSe Nanowires

The dynamics of the absorption bleaching in ZnSe can be varied by the presence of Ag NPs on the NW sidewalls. Both rise and decay times of the bleaching signal are affected by the presence of the Ag NPs. In particular, as shown in figure 9, the rise time increases from about 170 fs (see figure 9a) to about 250 fs (see figure 9b), while the decay time halves decreasing from 3.5 ps to 1.85 ps (see figure 9d). We notice here that no change in the dynamics of the bleaching signal is instead observed if Au NPs are formed on the ZnSe NW sidewalls (see figures 9c and 9d). As discussed above, electronic interaction between a semiconductor and a plasmonic NP mainly occurs through a number of pathways that depend upon the spatial proximity and the spectral overlap between the LSPR of the semiconductor transitions. The mechanisms based on direct

and indirect hot-carrier injection and FRET [62, 11], benefit from the proximity of the materials. However, for FRET, a necessary condition is the spectral overlap between the LSPR and the absorption band of the semiconductor [62]. In Ag-decorated ZnSe NWs, there are spectral overlaps and physical contact between the metal and the NW. This makes possible both FRET and hot-carrier transfer. In Au-decorated ZnSe NWs, where we have observed no change in the bleaching dynamics, there is contact between metal and NWs, but no spectral overlap between Au LSPR and ZnSe NBE absorption.

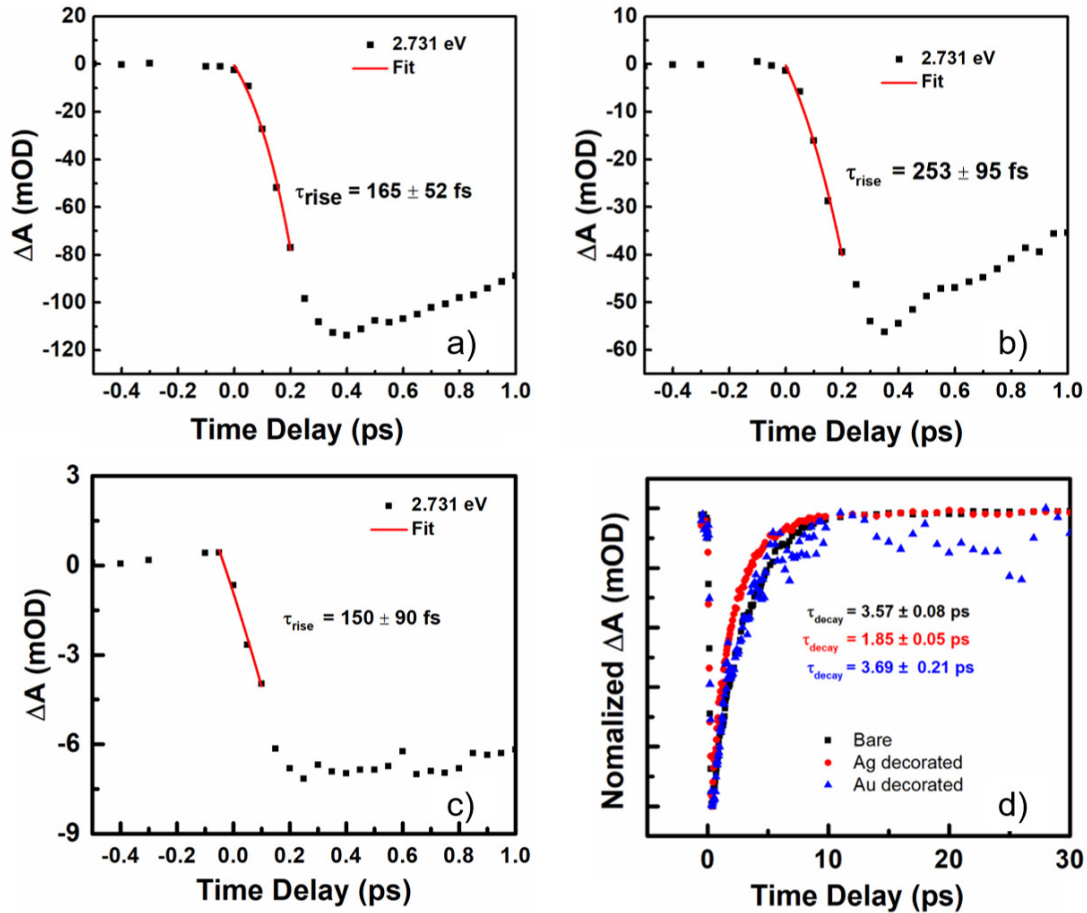


Figure 9 a) Rise time of near band-edge bleaching in bare ZnSe nanowires (ZnSe NWs), b) Rise time of near band-edge bleaching in Ag NP decorated ZnSe nanowires (AgNP@ZnSeNWs), c) Rise time of near band-edge bleaching in Au NP decorated ZnSe nanowires (AuNP@ZnSeNWs), and d) Comparison of the decay times of band edge bleaching in bare ZnSe NWs, AgNP@ZnSeNWs and AuNP@ZnSeNWs. These plots show how the AgNPs modify the dynamics of the ZnSe NW while the AuNPs do not.

The decay of the NP LSPR produces hot electrons in both Ag and Au NPs, whose energy distribution will reflect the density of states in the two metals. Because of the band alignment between the metals and ZnSe [63, 64], there are very close similarities between the Ag/ZnSe NW and Au/ZnSe NW interfaces and only part of the hot electrons will have energy above the ZnSe conduction band. Therefore, in the case the effects we observe in Ag-decorated ZnSe NWs were due to hot-carrier transfer, we should observe the same feature in Au-decorated ZnSe NWs but this is not the case. Hence, a resonant

mechanism must underlie the modifications observed with the formation of the Ag NPs on the NW sidewalls. In particular, the increase in the rise time of the bleaching signal points toward the presence of a FRET mechanism, where the Ag NPs act as donors and the ZnSe NWs are the acceptors [62, 11]. The increase of the rise time can be due to the excitation of electron-hole pairs in ZnSe at a later time than for direct photoexcitation, because of the energy transfer from the NPs toward the NWs.

Instead, a decrease of the decay time of the absorption bleaching is observed over the whole measured energy range. The absorption spectrum of the Ag NPs is very broad, due to the presence of both dipole and quadrupole excitation of the plasmon and, as shown above, of the shape distribution of the NPs [19, 65, 66]. At low energies, free-carrier absorption also contributes to their absorbance. The broad width may allow the resonant interaction with the defect band, with effects similar to those observed for the NBE. This resonant interaction with the defects, via an increased carrier-phonon scattering rate would explain the faster decay time in the TA signal of the Ag- decorated samples.

### 3.3.2. Silver Nanoparticles Embedded in CeO<sub>2</sub> Thin Films

The study of photocatalysis mediated by the LSPR has generated enormous interest in recent years due to the opportunity of extending the energy range of activity of traditional semiconductor photocatalysts when coupled with metallic nanoparticles [1, 3, 67, 68]. Among the semiconductor catalysts, cerium oxide (CeO<sub>2</sub>) is attracting growing interest due to its efficiency in catalyzing redox reactions [69, 70] thanks to the presence of localized Ce 4f states between the O 2p valence band and the Ce 5d conduction band [71]. In particular, we have used TA spectroscopy to investigate the mechanisms of LSPR decay in silver NPs embedded in a thin film of CeO<sub>2</sub> (Ag@CeO<sub>2</sub>).

Figure 10b shows the false-color map of TA spectra of the CeO<sub>2</sub> film without Ag NPs, excited with a pump at 275 nm (4.5 eV), above the optical gap of the semiconductor. The TA map is dominated by two features: a negative peak at 300 nm and a positive peak at 345 nm, showing only a slight decrease in intensity in the temporal window explored. This behavior suggests that the excited electrons are trapped in localized states [72]. The negative peak is assigned to the bleaching of the band edge, considering the band structure of CeO<sub>2</sub>, as schematically reported in Figure 10a. With this consideration in mind, we have assigned the positive peak to photoinduced absorption (PIA) from the Ce 4f levels into the Ce 5d band by the probe (see arrows in Figure 10a). When we excited Ag@CeO<sub>2</sub> with a pump at 275 nm, above the optical gap of CeO<sub>2</sub> and the inter-band transition of Ag NPs, we obtained a TA map with features related not only to the excited ceria but also to the transient plasmonic response of Ag NPs (data not shown [23]). In particular, the TA map presents a broad positive band around 610 nm and a broad negative band at 380-520 nm, associated with the transient line shape of the excited LSPR that presents the typical plasmonic decay dynamics in the first 10 ps similar to the TA response of the AuNPs in solution described above. These features are still clearly visible in the TA map also when we have excited the

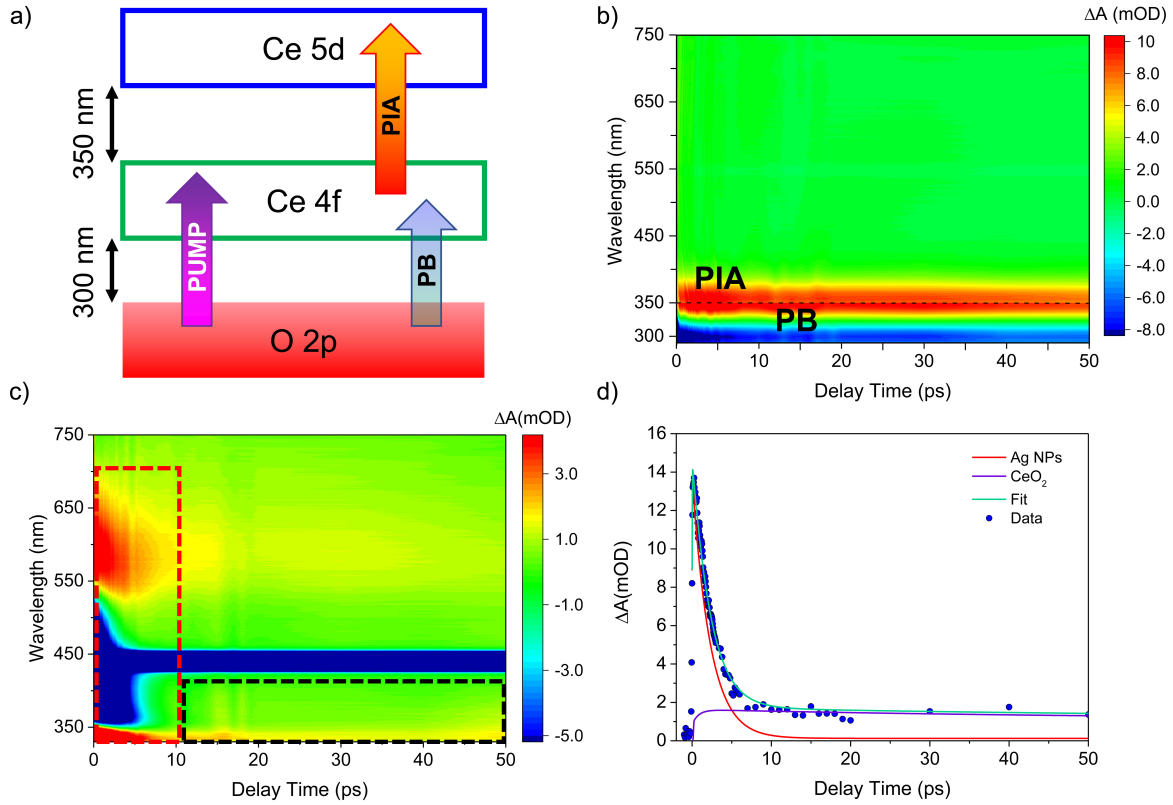


Figure 10 a) Sketch of the CeO<sub>2</sub> electronic structure, showing the transitions induced by the excitation of the pump at 275 nm and the corresponding TA signals (PB and PIA). b) False-color map of the TA spectra for the CeO<sub>2</sub> sample excited with a pump at 275 nm. The black dashed line at 350 nm separates the two sets of data acquired with the UV and Visible white light supercontinuum probes. c) False-color maps of the TA spectra of the Ag@CeO<sub>2</sub> sample excited with a pump at 440 nm, below the CeO<sub>2</sub> band gap and at LSPR maximum. The red dashed box indicates the part of the map dominated by the plasmonic response of the Ag NPs while the black dashed box delimits the PIA signal due to the electron injection into the CeO<sub>2</sub> film. The negative signal at 440 nm is due to scattering of the pump. d) Experimental time dependence of the transient PIA signal at 345 nm of the Ag@CeO<sub>2</sub> sample pumped at 440 nm. The components used for data fitting are shown as solid lines: PIA of CeO<sub>2</sub> (purple line); the plasmonic deexcitation (red line); the full fitting spectrum (green line).

sample with a pump at 440 nm, resonant with the LSPR and below the optical gap of CeO<sub>2</sub>, highlighted by the black dashed box in figure 10c. Moreover, even if the energy of the pump is not enough to excite the CeO<sub>2</sub> above the optical gap, the TA map of Ag@CeO<sub>2</sub> exhibits at time delays higher than 10 ps the same persistent signal at 345 nm assigned to PIA in CeO<sub>2</sub> (see red dashed box in Figure 10c). The presence of this signal has been assigned to transient occupation of 4f levels in ceria and is induced by LSPR-mediated electron injection.

The quantification of the efficiency of the electron injection was derived by comparing the PIA signal acquired at different pump energies. In particular, the temporal cuts of the TA maps at 345 nm were fitted by a linear combination of a contribution of the bare ceria, obtained from the thin film of CeO<sub>2</sub> [23], and



an exponentially decreasing function related to the positive signal generated by the excitation of the LSPR, as reported in Figure 10c for Ag@CeO<sub>2</sub> pumped at 440 nm. The signal related to the plasmonic dynamics dominates at delay times shorter than 5 ps, preventing the possibility to access the dynamics of the electron injection in this temporal region. For this reason, the quantification of the injection efficiency was obtained thanks to the TA signals at 345 nm of the Ag@CeO<sub>2</sub> sample pumped at different energies below the optical gap in the 50250 ps delay time range, where the LSPR-related signals are negligible [23]. The resulting injection efficiency values are in the range of 1216% for excitation between 400 and 500 nm, while a lower value of 6% is found for the pump at 600 nm [23]. As already discussed in the introduction, there are a number of mechanisms that can induce an electron injection mediated by the excitation of the LSPR, however in contrast to the previous example of AgNP@ZnSe NWs, the mechanisms that require an overlap between the LSPR and an optical transition in the semiconductor (light trapping, energy transfer to the semiconductor through near-field enhancement, plasmon induced radiative energy transfer and resonant energy transfer [73]) can be excluded because they cannot significantly contribute in this case. For this reason, the only mechanisms that are taken into consideration are the plasmon-induced indirect hot electron injection [1] and plasmon-induced direct electron injection [10, 74]. The efficiency of the indirect process is intrinsically limited by competition with electron thermalization that leads to a hot FermiDirac distribution in which most electrons do not have sufficient energy to overcome the Schottky barrier, and by the fact that the electrons need the moment vector directed towards the interface to be injected into the semiconductor. The combination of these two limitations means that, even in the most optimistic of estimates, a maximum of 8% injection efficiency can be achieved [75]. In contrast, the plasmon-induced direct carrier injection has been predicted to have efficiencies of between 40 and 50 % [74, 76] in TiO<sub>2</sub> sensitized with metal NPs. Furthermore the mechanism has been experimentally confirmed [10, 13] as a mechanism with a very high efficiency. For these reasons, we suggest that the high efficiencies of electron injection observed in the Ag@CeO<sub>2</sub> system are at least partly due to this direct mechanism [23]. Of course experimentally we cannot exclude the participation of the indirect mechanism and, indeed, to distinguish between these mechanisms would require experiments with resolution on the sub 10 fs timescale.

### *3.4. Alternative Method for Sensitization of Wide Band-Gap Semiconductors to Visible Light*

#### *3.4.1. V-doped TiO<sub>2</sub> Nanoparticles*

Ultrafast optical spectroscopy can also be used to investigate alternative methods to sensitize wide band-gap semiconductor materials to visible light which do not involve plasmonic materials. For example, a common technique to extend the absorption of TiO<sub>2</sub> into the visible range is to dope the material with a range of elements [77]. An example of this is our study of the charge carrier dynamics in undoped and vanadium-

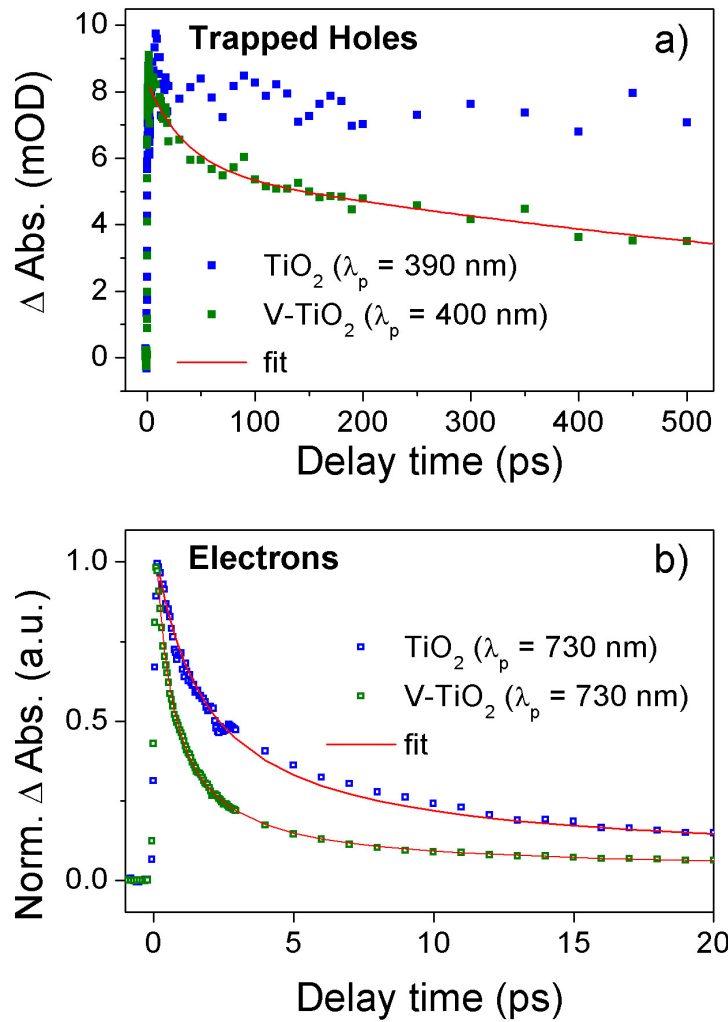


Figure 11 Observed dynamics following excitation of TiO<sub>2</sub> and V-TiO<sub>2</sub> NPs at a wavelength of 330 nm. a) dynamics of trapped holes, b) dynamics of photogenerated electrons. Both panels show the increased rate of recombination in the V-TiO<sub>2</sub> NPs in comparison to the TiO<sub>2</sub> NPs.

doped TiO<sub>2</sub> nanoparticles (TiO<sub>2</sub> and V-TiO<sub>2</sub> NPs, respectively) [78]. The aim of this work was to understand the link between the ultrafast charge carrier dynamics and the photocatalytic efficiency of the materials. To understand the effects of the doping on the carrier dynamics we recorded TA spectra of the NPs deposited on a quartz substrate in the 360-770 nm range following ultra bandgap excitation (330 nm) and near and sub bandgap excitation (400 nm and 520 nm). The transient spectra of TiO<sub>2</sub> have been extensively studied in the past [79, 80] and these studies guided our assignment of the observed spectral features of the TA: the peak at 400 nm was assigned to absorption of trapped holes, a monotonically increasing absorption towards the IR was assigned to free electron absorption and a TA band at 730 nm was assigned to absorption of trapped electrons. The latter signals were impossible to separate in our measurements and therefore we refer to the absorption at 730 nm as being due to both trapped and free electrons. The dynamics observed following ultraband gap excitation (see Figure

11) reveal a more rapid decay of the transient signals assigned both to trapped holes and to electrons in the V-TiO<sub>2</sub> NPs suggesting that the recombination mechanisms are promoted by the presence of the V defects. Near band gap excitation showed five times higher signals in the V-TiO<sub>2</sub> NPs samples for excited carriers while only the V-TiO<sub>2</sub> sample showed excited carrier signals for the sub band gap excitation.

These observations were correlated with the measurements of the internal photon conversion efficiency (IPCE) for photoelectrochemical water splitting of electrodes made with these materials. The IPCE of the TiO<sub>2</sub> NP based photoanodes is higher than the V-TiO<sub>2</sub> NP based photoanodes for photoexcitation wavelengths < 350 nm while the reverse is true for photoexcitation > 350 nm. This suggests that the increased recombination in the V-TiO<sub>2</sub> NPs following ultraband gap excitation leads to a decrease in the photoelectrocatalytic efficiency as the number of carriers available for photocatalysis is reduced while in the sub band gap excitation the increased absorption leads to a higher efficiency for the V-TiO<sub>2</sub> NPs. This demonstrates the contribution of the optical measurements of the carrier dynamics to the understanding the functional efficiency of materials.

#### 4. Conclusion and Perspectives

The optical pump-probe measurements described in this article illustrate the kinds of information on the photoexcited electron/carrier dynamics that can be accessed for nanostructured semiconductor and plasmonic materials using this technique. In the case of plasmonic gold NPs we have discussed how to follow the ultrafast relaxation processes which occur following plasmonic excitation by using the time dependent optical response of the materials. While in the case of the semiconductors we have discussed the band edge bleaching dynamics of ZnSe and Si NWs, and the morphological effects on hot-carrier cooling (hybrid organic inorganic perovskite thin film). Ideally what is required in a hybrid system, in which the absorption cross-section of the plasmonic material is used to sensitize the semiconductor to the exciting light, is that energy is transferred from the plasmonic material before the energy is lost to these ultrafast processes and is ultimately dissipated as heat. In this work we discussed two examples in which such ultrafast energy transfer occurs: i) Ag NPs on ZnSe NWs in which the spectral overlap of the plasmon resonance and the band gap of the semiconductor allows energy transfer to occur via the FRET mechanism and ii) Ag NPs embedded in a CeO<sub>2</sub> thin film in which we detected a highly efficient charge transfer following plasmonic excitation of the Ag NPs to long-lived states in the CeO<sub>2</sub> film. Finally, an alternative method of extending the absorption of a wide band semiconductor into the visible range is discussed based on the doping of TiO<sub>2</sub> NPs with vanadium and the subsequent effect on carrier dynamics and photoelectrocatalytic efficiency.

As can be seen from the above examples of hybrid plasmonic/semiconductor materials the energy transfer occurs on an ultrafast timescale and clearly ultrafast techniques such as the one described here are required to study such processes. On

the other hand, the desired photoinduced functional properties of the materials often take place under continuous wave excitation (solar cells, catalysis) and therefore it can be difficult to directly relate the ultrafast processes to the efficiencies of devices based on these materials. For example, catalysis can take place on the microsecond to second timescale and therefore in future experiments it will be important to bridge the temporal gap by correlating the ultrafast processes with improved performance of the material on the long timescales required for improved functionality. An example of this kind of approach can be found in our study of the  $\text{TiO}_2$  and V- $\text{TiO}_2$  described above, however, this approach is not widely employed in the literature. Indeed, this has been identified as one of the reasons for the lack of technological advance in photocatalytic water treatment in spite of great deal of “initial academic hype” on high energy transfer efficiencies [81].

Another interesting area of research which is little explored in the literature is the investigation of the effects of externally applied fields on interface transfer dynamics. External fields can modify band alignment and barriers at the interfaces thus strongly modifying charge transfer processes. Such modified transfer efficiencies will certainly be more relevant to the operational efficiency of devices which involve the external application of fields such as solar cells and photoelectrocatalysis.

Finally, other future research will be aimed at understanding the combined effect of plasmonically generated charge transfer and the thermal effects due to losses in the plasmonic material on photocatalytic efficiency. In the recent literature there has been significant debate on which of these mechanisms dominates in plasmonically assisted photocatalysis in metallic plasmon materials [82, 83, 84]. Obtaining a synergy between the two mechanisms [85] may lead to higher overall efficiency the hybrid systems discussed in this work.

## 5. Acknowledgements

This work has received funding from the European Unions 7th Framework Programme for research, technological development, and demonstration under Grant No. 316751 (NanoEmbrace) and from the Horizon 2020 program of the European Union for research and innovation, under grant agreement no. 722176 (INDEED). We thank Silvia Rubini and Valentina Zannier (IOM-CNR, Trieste) for providing the ZnSe NWs, Francesco Bisio (SPIN-CNR) for providing the 2D arrays of NPs, Federico Boscherini and Luca Pasquini (University of Bologna) for supplying the  $\text{TiO}_2$  NPs, Iole Venditti (Roma Tre University) and Ilaria Fratoddi (Roma Tre and “La Sapienza” University) for the Au NPs in solution, Paola Luches (NANO-CNR) and Sergio D’Addato (UniMore) for the Ag@Ceria films, Aldo DiCarlo, Antonio Agresti and Pescetelli (Tor Vergata University) for the perovskite samples, Bruno Palpant (LPQM) and Remo Proietti Zaccaria (IIT) for theoretical support and Davide Sangalli and Andrea Marini (ISM-CNR) for very fruitful discussions.

This is the version of the article before peer review or editing, as submitted by an author to Nanotechnology. IOP Publishing Ltd is not responsible for any errors or

omissions in this version of the manuscript or any version derived from it. The Version of Record is available online at <https://doi.org/10.1088/1361-6528/abb907>

## 6. References

- [1] Clavero C 2014 *Nature Photonics* **8** 95–103 URL <https://doi.org/10.1038/nphoton.2013.238>
- [2] Liu L, Zhang X, Yang L, Ren L, Wang D and Ye J 2017 *National Science Review* **4** 761–780 URL <https://doi.org/10.1093/nsr/nwx019>
- [3] Zhang Y, He S, Guo W, Hu Y, Huang J, Mulcahy J R and Wei W D 2018 *Chemical Reviews* **118** 2927–2954 URL <https://doi.org/10.1021/acs.chemrev.7b00430>
- [4] Valenti M, Jonsson M P, Biskos G, Schmidt-Ott A and Smith W A 2016 *J. Mater. Chem. A* **4**(46) 17891–17912 URL <http://dx.doi.org/10.1039/C6TA06405A>
- [5] Wu N 2018 *Nanoscale* **10**(6) 2679–2696 URL <http://dx.doi.org/10.1039/C7NR08487K>
- [6] Galán-González A, Sivan A K, Hernández-Ferrer J, Bowen L, Di Mario L, Martelli F, Benito A M, Maser W K, Chaudhry M U, Gallant A, Zeze D A and Atkinson D O *ACS Applied Nano Materials* **0** null URL <https://doi.org/10.1021/acsanm.0c01325>
- [7] Tang H, Chen C J, Huang Z, Bright J, Meng G, Liu R S and Wu N 2020 *The Journal of Chemical Physics* **152** 220901 URL <https://doi.org/10.1063/5.0005334>
- [8] Stockman M I 2011 *Opt. Express* **19** 22029–22106 URL <http://www.opticsexpress.org/abstract.cfm?URI=oe-19-22-22029>
- [9] Jain P K, Lee K S, El-Sayed I H and El-Sayed M A 2006 *The Journal of Physical Chemistry B* **110** 7238–7248 URL <https://doi.org/10.1021/jp057170o>
- [10] Wu K, Chen J, McBride J R and Lian T 2015 *Science* **349** 632–635 URL <https://science.sciencemag.org/content/349/6248/632>
- [11] Li J, Cushing S K, Meng F, Senty T R, Bristow A D and Wu N 2015 *Nature Photonics* **9** 601–607 URL <https://doi.org/10.1038/nphoton.2015.142>
- [12] Khurgin J B 2019 *Faraday Discuss.* **214**(0) 35–58 URL <http://dx.doi.org/10.1039/C8FD00200B>
- [13] Tan S, Argondizzo A, Ren J, Liu L, Zhao J and Petek H 2017 *Nature Photonics* **11** 806–812 URL <https://doi.org/10.1038/s41566-017-0049-4>
- [14] Hartland G V 2011 *Chemical Reviews* **111** 3858–3887 URL <https://doi.org/10.1021/cr1002547>
- [15] Othonos A 1998 *Journal of Applied Physics* **83** 1789–1830 URL <https://doi.org/10.1063/1.367411>
- [16] Fratoddi I, Cartoni A, Venditti I, Catone D, O’Keeffe P, Paladini A, Toschi F, Turchini S, Sciubba F, Testa G, Battocchio C, Carlini L, Zaccaria R P, Magnano E, Pis I and Avaldi L 2018 *Journal of Colloid and Interface Science* **513** 10 – 19 URL <http://www.sciencedirect.com/science/article/pii/S0021979717312961>
- [17] Catone D, Ciavardini A, Di Mario L, Paladini A, Toschi F, Cartoni A, Fratoddi I, Venditti I, Alabastri A, Proietti Zaccaria R and O’Keeffe P 2018 *The Journal of Physical Chemistry Letters* **9** 5002–5008 URL <https://doi.org/10.1021/acs.jpcllett.8b02117>
- [18] Magnozzi M, Proietti Zaccaria R, Catone D, O’Keeffe P, Paladini A, Toschi F, Alabastri A, Canepa M and Bisio F 2019 *The Journal of Physical Chemistry C* **123** 16943–16950 URL <https://doi.org/10.1021/acs.jpcc.9b03668>
- [19] Di Mario L, Otomalo T O, Catone D, O’Keeffe P, Tian L, Turchini S, Palpant B and Martelli F 2018 *Phys. Rev. B* **97**(11) 115448 URL <https://link.aps.org/doi/10.1103/PhysRevB.97.115448>
- [20] Tian L, di Mario L, Zannier V, Catone D, Colonna S, O’Keeffe P, Turchini S, Zema N, Rubini S and Martelli F 2016 *Phys. Rev. B* **94**(16) 165442 URL <https://link.aps.org/doi/10.1103/PhysRevB.94.165442>
- [21] Tian L, Mario L D, Sivan A K, Catone D, O’Keeffe P, Paladini A, Turchini S and Martelli F 2019 *Nanotechnology* **30** 214001
- [22] O’Keeffe P, Catone D, Paladini A, Toschi F, Turchini S, Avaldi L, Martelli F, Agresti A, Pescetelli

- S, Del Rio Castillo A E, Bonaccorso F and Di Carlo A 2019 *Nano Letters* **19** 684–691 URL <https://doi.org/10.1021/acs.nanolett.8b03685>
- [23] Cresi J S P, Spadaro M C, D’Addato S, Valeri S, Benedetti S, Bona A D, Catone D, Mario L D, O’Keeffe P, Paladini A, Bertoni G and Luches P 2019 *Nanoscale* **11** 10282–10291
- [24] Sivan A K, Mario L D, Catone D, O’Keeffe P, Turchini S, Rubini S and Martelli F 2020 *Nanotechnology* **31** 174001 URL <https://doi.org/10.1088%2F1361-6528%2F174001>
- [25] Ahmadi T S, Logunov S L and El-Sayed M A 1996 *The Journal of Physical Chemistry* **100** 8053–8056 URL <https://pubs.acs.org/doi/10.1021/jp960484e>
- [26] Hartland G V 2004 *Physical Chemistry Chemical Physics* **6** 5263 URL <https://pubs.rsc.org/en/content/articlelanding/2004/CP/b413368d#!divAbstract>
- [27] El-Sayed M A 2001 *Accounts of Chemical Research* **34** 257–264 URL <https://pubs.acs.org/doi/10.1021/ar960016n>
- [28] Murphy C J, Sau T K, Gole A M, Orendorff C J, Gao J, Gou L, Hunyadi S E and Li T 2005 *The Journal of Physical Chemistry B* **109** 13857–13870
- [29] Kravets A F, Borodinova T I and Kravets V G 2016 *Journal of the Optical Society of America B* **33** 302
- [30] Kojima C, Watanabe Y, Hattori H and Iida T 2011 *The Journal of Physical Chemistry C* **115** 19091–19095
- [31] Ghosh S K and Pal T 2007 *Chemical Reviews* **107** 4797–4862 URL <https://pubs.acs.org/doi/10.1021/cr0680282>
- [32] Jain P K and El-Sayed M A 2010 *Chemical Physics Letters* **487** 153–164
- [33] Convertino A, Cuscunà M, Martelli F, Manera M G and Rella R 2014 *The Journal of Physical Chemistry C* **118** 685–690 URL <https://doi.org/10.1021/jp411743p>
- [34] Guillet Y, Rashidi-Huyeh M and Palpant B 2009 *Phys. Rev. B* **79**(4) 045410 URL <https://link.aps.org/doi/10.1103/PhysRevB.79.045410>
- [35] Guillet Y, Charron E and Palpant B 2009 *Phys. Rev. B* **79**(19) 195432 URL <https://link.aps.org/doi/10.1103/PhysRevB.79.195432>
- [36] Baida H, Mongin D, Christofilos D, Bachelier G, Crut A, Maioli P, Del Fatti N and Vallée F 2011 *Phys. Rev. Lett.* **107**(5) 057402 URL <https://link.aps.org/doi/10.1103/PhysRevLett.107.057402>
- [37] Baffou G and Quidant R 2013 *Laser & Photonics Reviews* **7** 171–187 URL <https://onlinelibrary.wiley.com/doi/abs/10.1002/lpor.201200003>
- [38] Zavelani-Rossi M, Polli D, Kochtchev S, Baudrion A L, Bal J, Kumar V, Molotokaite E, Marangoni M, Longhi S, Cerullo G, Adam P M and Della Valle G 2015 *ACS Photonics* **2** 521–529 URL <https://doi.org/10.1021/ph5004175>
- [39] Ferrera M, Della Valle G, Sygletou M, Magnozzi M, Catone D, O’Keeffe P, Paladini A, Toschi F, Mattera L, Canepa M and Bisio F 2020 *ACS Photonics* **7** 959–966 URL <https://doi.org/10.1021/acsp Photonics.9b01605>
- [40] Anghinolfi L, Mattera L, Canepa M and Bisio F 2012 *Phys. Rev. B* **85**(23) 235426 URL <https://link.aps.org/doi/10.1103/PhysRevB.85.235426>
- [41] Harutyunyan H, Martinson A B F, Rosenmann D, Khorashad L K, Besteiro L V, Govorov A O and Wiederrecht G P 2015 *Nature Nanotechnology* **10** 770–774 URL <https://doi.org/10.1038/nnano.2015.165>
- [42] Boulais É, Lachaine R and Meunier M 2012 *Nano Letters* **12** 4763–4769 URL <https://doi.org/10.1021/nl302200w>
- [43] Hobbs R G, Putnam W P, Fallahi A, Yang Y, Körtner F X and Berggren K K 2017 *Nano Letters* **17** 6069–6076 URL <https://doi.org/10.1021/acs.nanolett.7b02495>
- [44] Hu M, Petrova H and Hartland G V 2004 *Chemical Physics Letters* **391** 220–225
- [45] Weiland T 1977 *Archiv Elektronik und Uebertragungstechnik* **31** 116–120 URL <https://ui.adsabs.harvard.edu/abs/1977ArElU...31..116W>
- [46] Zuo L, Gu Z, Ye T, Fu W, Wu G, Li H and Chen H 2015 *Journal of the American Chemical*



- Society* **137** 2674–2679 URL <https://doi.org/10.1021/ja512518r>
- [47] Fakharuddin A, Schmidt-Mende L, Garcia-Belmonte G, Jose R and Mora-Sero I 2017 *Advanced Energy Materials* **7** 1700623 URL <https://onlinelibrary.wiley.com/doi/abs/10.1002/aenm.201700623>
- [48] Saliba M, Matsui T, Seo J Y, Domanski K, Correa-Baena J P, Nazeeruddin M K, Zakeeruddin S M, Tress W, Abate A, Hagfeldt A and Grtzel M 2016 *Energy Environ. Sci.* **9**(6) 1989–1997 URL <http://dx.doi.org/10.1039/C5EE03874J>
- [49] Asghar M, Zhang J, Wang H and Lund P 2017 *Renewable and Sustainable Energy Reviews* **77** 131 – 146 URL <http://www.sciencedirect.com/science/article/pii/S1364032117304756>
- [50] D’Innocenzo V, Grancini G, Alcocer M J P, Kandada A R S, Stranks S D, Lee M M, Lanzani G, Snaith H J and Petrozza A 2014 *Nature Communications* **5** 3586 URL <https://doi.org/10.1038/ncomms4586>
- [51] Yang Y, Ostrowski D P, France R M, Zhu K, van de Lagemaat J, Luther J M and Beard M C 2016 *Nature Photonics* **10** 53–59 URL <https://doi.org/10.1038/nphoton.2015.213>
- [52] Yang J, Wen X, Xia H, Sheng R, Ma Q, Kim J, Tapping P, Harada T, Kee T W, Huang F, Cheng Y B, Green M, Ho-Baillie A, Huang S, Shrestha S, Patterson R and Conibeer G 2017 *Nature Communications* **8** 14120 URL <https://doi.org/10.1038/ncomms14120>
- [53] Street R A, Qi P, Lujan R and Wong W S 2008 *Applied Physics Letters* **93** 163109 URL <https://doi.org/10.1063/1.3005585>
- [54] Street R A, Wong W S and Paulson C 2009 *Nano Letters* **9** 3494–3497 URL <https://doi.org/10.1021/nl901683y>
- [55] Convertino A, Cuscutà M and Martelli F 2010 *Nanotechnology* **21** 355701 URL <https://doi.org/10.1088%2F0957-4484%2F21%2F35%2F355701>
- [56] Convertino A, Cuscutà M, Rubini S and Martelli F 2012 *Journal of Applied Physics* **111** 114302 URL <https://doi.org/10.1063/1.4723567>
- [57] Zannier V, Martelli F, Grillo V, Plaisier J R, Lausi A and Rubini S 2014 *physica status solidi (RRL) Rapid Research Letters* **8** 182–186 URL <https://onlinelibrary.wiley.com/doi/abs/10.1002/pssr.201308264>
- [58] Tian L, Mario L D, Minotti A, Tiburzi G, Mendis B G, Zeze D A and Martelli F 2016 *Nanotechnology* **27** 225601 URL <https://doi.org/10.1088%2F0957-4484%2F27%2F22%2F225601>
- [59] Imai K, Kumazaki K, Haga T and Abe Y 1988 *Journal of Crystal Growth* **91** 617 – 622 URL <http://www.sciencedirect.com/science/article/pii/0022024888901303>
- [60] Sangalli D, Dal Conte S, Manzoni C, Cerullo G and Marini A 2016 *Phys. Rev. B* **93**(19) 195205 URL <https://link.aps.org/doi/10.1103/PhysRevB.93.195205>
- [61] Schultze M, Ramasesha K, Pemmaraju C, Sato S, Whitmore D, Gandman A, Prell J S, Borja L J, Prendergast D, Yabana K, Neumark D M and Leone S R 2014 *Science* **346** 1348–1352 URL <https://science.sciencemag.org/content/346/6215/1348>
- [62] Th F 1965 *Modern Quantum Chemistry* (New York: Academic)
- [63] Vos M, Xu F, Anderson S G, Weaver J H and Cheng H 1989 *Phys. Rev. B* **39**(15) 10744–10752 URL <https://link.aps.org/doi/10.1103/PhysRevB.39.10744>
- [64] Pelucchi E, Kumar D, Lazzarino M, Rubini S and Franciosi A 2006 *Journal of Vacuum Science & Technology B: Microelectronics and Nanometer Structures Processing, Measurement, and Phenomena* **24** 1259–1265 URL <https://avs.scitation.org/doi/abs/10.1116/1.2194944>
- [65] Kelly K L, Coronado E, Zhao L L and Schatz G C 2003 *The Journal of Physical Chemistry B* **107** 668–677 URL <https://doi.org/10.1021/jp026731y>
- [66] Liu X, Li D, Sun X, Li Z, Song H, Jiang H and Chen Y 2015 *Scientific Reports* **5** 12555 URL <https://doi.org/10.1038/srep12555>
- [67] Kale M J, Avanesian T and Christopher P 2014 *ACS Catalysis* **4** 116–128 URL <https://doi.org/10.1021/cs400993w>
- [68] Narang P, Sundararaman R and Atwater H A 2016 *Nanophotonics* **5** 96 – 111 URL <https://doi.org/10.1515/nanoph-2016-0011>

- [//www.degruyter.com/view/journals/nanoph/5/1/article-p96.xml](http://www.degruyter.com/view/journals/nanoph/5/1/article-p96.xml)
- [69] Navalon S, de Miguel M, Martin R, Alvaro M and Garcia H 2011 *Journal of the American Chemical Society* **133** 2218–2226 URL <https://doi.org/10.1021/ja108816p>
- [70] Lei W, Zhang T, Gu L, Liu P, Rodriguez J A, Liu G and Liu M 2015 *ACS Catalysis* **5** 4385–4393 URL <https://doi.org/10.1021/acscatal.5b00620>
- [71] Skorodumova N V, Simak S I, Lundqvist B I, Abrikosov I A and Johansson B 2002 *Phys. Rev. Lett.* **89**(16) 166601 URL <https://link.aps.org/doi/10.1103/PhysRevLett.89.166601>
- [72] Pelli Cresi J S, Di Mario L, Catone D, Martelli F, Paladini A, Turchini S, DAddato S, Luches P and O’Keeffe P 2020 *The Journal of Physical Chemistry Letters* **11** 5686–5691 URL <https://doi.org/10.1021/acs.jpcllett.0c01590>
- [73] Atwater H A and Polman A 2010 *Nature Materials* **9** 205–213 URL <https://doi.org/10.1038/nmat2629>
- [74] Long R and Prezhdo O V 2014 *Journal of the American Chemical Society* **136** 4343–4354 URL <https://doi.org/10.1021/ja5001592>
- [75] White T P and Catchpole K R 2012 *Applied Physics Letters* **101** 073905 URL <https://doi.org/10.1063/1.4746425>
- [76] Ma J and Gao S 2019 *ACS Nano* **13** 13658–13667 URL <https://doi.org/10.1021/acsnano.9b03555>
- [77] Pelaez M, Nolan N T, Pillai S C, Seery M K, Falaras P, Kontos A G, Dunlop P S, Hamilton J W, Byrne J, O’Shea K, Entezari M H and Dionysiou D D 2012 *Applied Catalysis B: Environmental* **125** 331–349 URL <http://www.sciencedirect.com/science/article/pii/S0926337312002391>
- [78] Rossi G, Pasquini L, Catone D, Piccioni A, Patelli N, Paladini A, Molinari A, Caramori S, O’Keeffe P and Boscherini F 2018 *Applied Catalysis B: Environmental* **237** 603–612 URL <http://www.sciencedirect.com/science/article/pii/S092633731830537X>
- [79] Yoshihara T, Katoh R, Furube A, Tamaki Y, Murai M, Hara K, Murata S, Arakawa H and Tachiya M 2004 *The Journal of Physical Chemistry B* **108** 3817–3823 URL <https://doi.org/10.1021/jp031305d>
- [80] Tamaki Y, Furube A, Murai M, Hara K, Katoh R and Tachiya M 2007 *Phys. Chem. Chem. Phys.* **9**(12) 1453–1460 URL <http://dx.doi.org/10.1039/B617552J>
- [81] Loeb S K, Alvarez P J J, Brame J A, Cates E L, Choi W, Crittenden J, Dionysiou D D, Li Q, Li-Puma G, Quan X, Sedlak D L, David Waite T, Westerhoff P and Kim J H 2019 *Environmental Science & Technology* **53** 2937–2947 URL <https://doi.org/10.1021/acs.est.8b05041>
- [82] Dubi Y and Sivan Y 2019 *Light: Science & Applications* **8** 89 URL <https://doi.org/10.1038/s41377-019-0199-x>
- [83] Dubi Y, Un I W and Sivan Y 2020 *Chem. Sci.* **11**(19) 5017–5027 URL <http://dx.doi.org/10.1039/C9SC06480J>
- [84] Gargiulo J, Bert R, Li Y, Maier S A and Corts E 2019 *Accounts of Chemical Research* **52** 2525–2535 URL <https://doi.org/10.1021/acs.accounts.9b00234>
- [85] Li X, Everitt H O and Liu J 2020 *Nano Research* **13** 1268–1280 URL <https://doi.org/10.1007/s12274-020-2694-z>